

# Dynamic stabilization of the optical resonances of single nitrogen-vacancy centers in diamond

V. M. Acosta,<sup>1,\*</sup> C. Santori,<sup>1</sup> A. Faraon,<sup>1</sup> Z. Huang,<sup>1</sup> K.-M. C. Fu,<sup>1</sup> A. Stacey,<sup>2</sup>  
D. A. Simpson,<sup>2</sup> S. Tomljenovic-Hanic,<sup>2</sup> A. D. Greentree,<sup>2</sup> S. Prawer,<sup>2</sup> and R. G. Beausoleil<sup>1</sup>

<sup>1</sup>*Hewlett-Packard Laboratories, 1501 Page Mill Rd., Palo Alto, CA 94304*

<sup>2</sup>*School of Physics, University of Melbourne, Parkville, Melbourne VIC 3010, Australia*

We report electrical tuning by the Stark effect of the excited-state structure of single nitrogen-vacancy (NV) centers located  $\lesssim 100$  nm from the diamond surface. The zero-phonon line (ZPL) emission frequency is controllably varied over a range of 300 GHz. Using high-resolution emission spectroscopy, we observe electrical tuning of the strengths of both cycling and spin-altering transitions. Under resonant excitation, we apply dynamic feedback to stabilize the ZPL frequency, nearly eliminating spectral diffusion on timescales  $\gtrsim 50$  ms.

Integrated photonic networks based on cavity-coupled solid-state spin impurities offer a promising platform for scalable quantum computing [1–5]. A key ingredient for this technology is the generation and interference of indistinguishable photons emitted by pairs of identical spin qubits [6–8]. This requires spectrally stable emitters with identical level structure, a formidable challenge in the solid-state environment.

A potential solution is to use external control to counteract sample inhomogeneities. In candidate systems based on single molecules [9–11], quantum dots [12, 13], and negatively-charged nitrogen-vacancy (NV) centers in diamond [1, 2, 14], the level structure can be statically tuned via the DC Stark effect. However, the spectral stability of emitters in these systems is often hampered by local fluctuations which cause the emission frequency to change with time, a phenomenon known as spectral diffusion [17]. Previous attempts to address this problem have focused on improving the host material [14, 18–20] or using post-selection techniques [2, 21–23], but a robust, high-yield solution is still lacking.

The diamond NV center is a particularly attractive spin qubit, as it exhibits a unique combination of long-lived spin coherence [24] and efficient optical control and readout [25, 26]. However integration into on-chip photonic networks requires NV centers to be located near nanostructured diamond surfaces, where inhomogeneous strain and spectral diffusion can be particularly problematic [27, 28]. In this Letter, we first demonstrate electrical control over the zero-phonon line (ZPL) transition frequencies, as well as probabilities for both cycling and  $\Lambda$ -type transitions, of single NV centers located near the diamond surface. We then show that spectral diffusion of the ZPL can be virtually eliminated for timescales  $\gtrsim 50$  ms by providing rapid electrical feedback to compensate for local field fluctuations. Applied simultaneously to a pair of NV centers, these techniques pave the way for increased two-photon interference visibilities [2, 11, 13] and heralded entanglement success probabilities [8].

The diamond NV center consists of a substitutional nitrogen impurity adjacent to a carbon vacancy. The

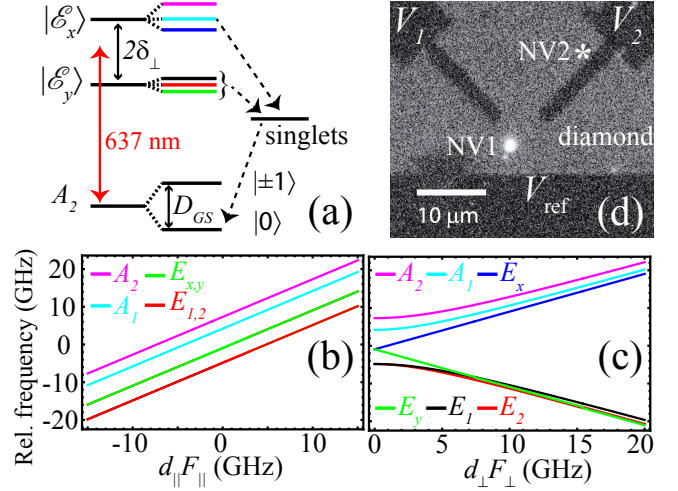


FIG. 1. (a) NV level structure at high transverse electric field ( $d_{\perp}F_{\perp} \equiv \delta_{\perp} > 15$  GHz). The dashed line indicates the spin-selective decay path responsible for optical pumping. (b) Effect of longitudinal and (c) transverse electric fields on the excited state levels, as described in the text. The angle of the transverse field is  $\theta_r = 15^\circ$  from a  $C_{3v}$  reflection plane. (d) Fluorescence micrograph of the electrode structure used here. NV1 was illuminated by 532 nm light and appears white, while the position of NV2 is denoted with an asterisk. Metal electrodes appear as shadows.

center has  $C_{3v}$  symmetry, and the basic energy structure is depicted in Fig. 1(a). The spin-triplet ground state,  $^3A_2$ , is split such that the  $m_s = 0$  spin projection (labeled  $|0\rangle$  throughout) is separated from the degenerate  $m_s = \pm 1$  levels ( $|\pm 1\rangle$ ) by  $D_{GS} = 2.88$  GHz at  $T \lesssim 100$  K [29]. The optically excited state (ES) is a spin triplet and orbital doublet with  $^3E$  symmetry, and its fine structure has been studied theoretically in detail [30, 31]. The Hamiltonian describing the ES manifold is:

$$\begin{aligned}\mathcal{H}_{ES} &= \mathcal{H}_{SO} + \mathcal{H}_{SS} + \mathcal{H}_{Stark}, \\ \mathcal{H}_{Stark} &= -\vec{d} \cdot \vec{F},\end{aligned}\quad (1)$$

where  $\mathcal{H}_{SO}$ ,  $\mathcal{H}_{SS}$ , and  $\mathcal{H}_{Stark}$  contain respectively, the spin-orbit, spin-spin, and Stark effect contributions;  $\vec{d}$

is the electric dipole moment, and  $\vec{F}$  is the electric field. The effect of a local strain field is treated by rewriting strain as an effective electric field [32, 33].

We first consider the influence of  $\mathcal{H}_{Stark}$  on only the spatial portion of the ES wavefunction, which is composed of two orthogonal orbitals that are degenerate in the absence of external fields. In the presence of an electric field, the orbital eigenstates, labeled  $\{|\mathcal{E}_x\rangle, |\mathcal{E}_y\rangle\}$ , undergo energy shifts,  $\Delta(\vec{F})$ , of:

$$\begin{aligned}\Delta_{\mathcal{E}_x}(\vec{F}) &= d_{\parallel}F_{\parallel} + d_{\perp}F_{\perp}, \\ \Delta_{\mathcal{E}_y}(\vec{F}) &= d_{\parallel}F_{\parallel} - d_{\perp}F_{\perp},\end{aligned}\quad (2)$$

where the directions are with respect to the NV symmetry axis. Longitudinal fields do not lift the orbital degeneracy, and result only in equal, linear shifts of all levels. Transverse fields split the orbitals into two branches with an energy difference,  $2\delta_{\perp} \equiv (\Delta_{\mathcal{E}_x} - \Delta_{\mathcal{E}_y})$ , that grows linearly with increasing field. The spacings between ground-state sublevels remain largely unaffected by electric fields [34, 35]. While the ground state might have a non-zero longitudinal dipole moment,  $d_{GS,\parallel}$  [30, 31], only the difference  $d_{\parallel} - d_{GS,\parallel}$  is resolved in our experiments, so we take  $d_{GS,\parallel} = 0$  throughout.

Incorporating spin interactions results in a set of six eigenstates,  $\{|A_2\rangle, |A_1\rangle, |E_x\rangle, |E_y\rangle, |E_1\rangle, |E_2\rangle\}$ , ordered from highest to lowest energy (at low field). Figures 1(b) and (c) show the effect of  $\mathcal{H}_{ES}$  on all six ES energies due to, respectively,  $F_{\parallel}$  and  $F_{\perp}$ . As will be discussed, an important feature is the presence of transverse-field-dependent avoided crossings amongst levels in the lower orbital branch, comprised of  $\{|E_y\rangle, |E_1\rangle, |E_2\rangle\}$ .

We focused our study on NV centers in close proximity to the diamond surface, a necessary feature for future integration with nanophotonic devices. The diamond sample is described in detail elsewhere [36]. It consists of a single-crystal, [100]-oriented diamond substrate, with nitrogen content less than  $10^{15} \text{ cm}^{-3}$ . The top  $\sim 50 \text{ }\mu\text{m}$  of the substrate has been plasma treated [37] so as to exhibit virtually no NV fluorescence. An approximately 100 nm layer of diamond was grown on top of this substrate and the resulting sheet density of  $\text{NV}^-$  centers is  $\sim 10^6 \text{ cm}^{-2}$ . The two NV centers studied in this work, labeled NV1 and NV2, are expected to be in this overgrown layer [36]. Lithographically-defined metal electrodes [1] were deposited on the overgrown diamond layer [Fig. 1(d)]. The layout of the electrodes (labeled  $V_1$ ,  $V_2$  and  $V_{\text{ref}}$ ) permits tuning of electric fields in any in-plane direction near the center of the structure. Electrostatic modeling of the structure can be found in [Supplementary Information].

Experiments were performed with a confocal microscope, which was used to excite and collect emitted light from a diamond sample in thermal contact with the cold finger of a flow-through, liquid-helium cryo-

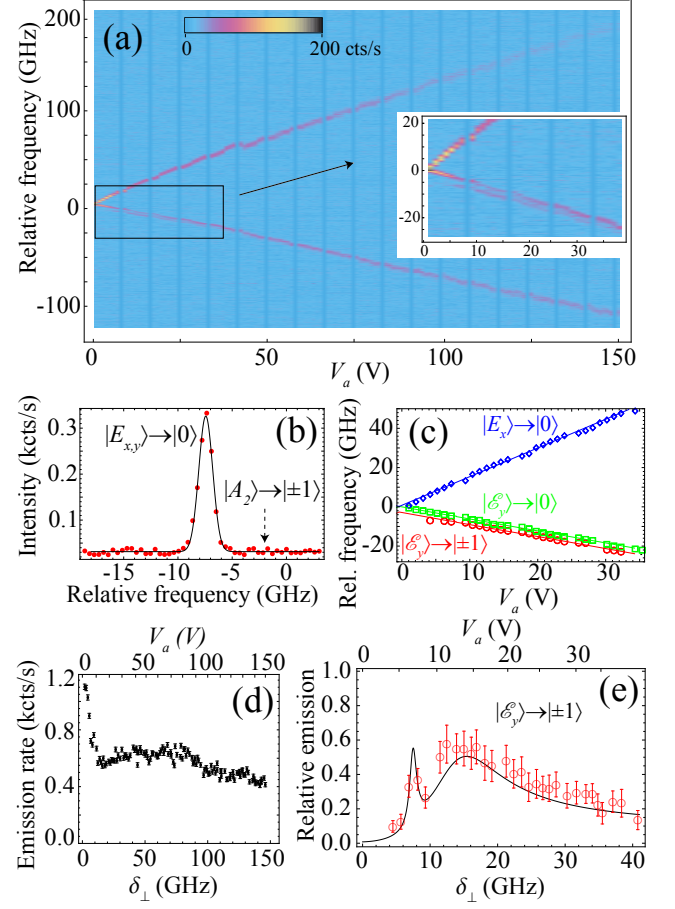


FIG. 2. (a) Stark emission spectroscopy data set.  $V_a$  was scanned at a rate of 1 V/min and emission spectra were obtained by integrating over one-minute intervals. A dark exposure frame was taken every 8th frame (cyan vertical stripes). Emission frequencies are relative to 470.45 THz (637.25 nm). Low-field data are inset. (b) Emission spectrum for  $V_a = 1$  V with expected peak positions labeled. The  $|E_{x,y}\rangle \rightarrow |0\rangle$  emission line is fit with a Gaussian profile. (c) Low-field peak positions determined from Lorentzian fits (symbols), and a global fit to the model based on Eq. (1). Lorentzian fit uncertainty is smaller than the plotted symbols. (d) Total ZPL emission versus  $\delta_{\perp}$ . The emission rate was calculated by subtracting the mean background and summing counts over a range of  $\sim 3$  FWHM linewidths centered at each peak. The error bars are based on Poissonian noise. (e) Relative intensity of the  $|\mathcal{E}_y\rangle \rightarrow |\pm 1\rangle$  emission line along with fit (see text). The intensities and error were determined from Lorentzian fits to the two partially-resolved emission lines.

stat. The cold finger was maintained at a temperature  $T \approx 7$  K, and no magnetic field was applied. Two forms of spectroscopy were employed: high-resolution emission spectroscopy and photoluminescence excitation spectroscopy.

For emission spectroscopy, 2 mW of light from a 532-nm solid-state laser was focused by a 0.6-numerical-aperture objective onto NV1, exciting through the phonon sideband (PSB). The collected emission was

spectrally filtered to direct ZPL light (636-638 nm) to a high-resolution grating spectrometer. The optical polarization was chosen to ensure excitation of both orbital branches [38]. Figure 2(a) shows the emission spectra versus voltage,  $V_a$ , applied simultaneously on  $V_1$  and  $V_{\text{ref}}$ , with  $V_2 = 0$ . By varying  $V_a$  from 0 to 150 V, we observe linear tuning of emission lines over a range exceeding 300 GHz. Such a wide tuning range is essential to compensate for the large intrinsic fields typical in nanophotonic devices [28].

Depending on the applied voltage, we resolve between one and three emission lines. At  $V_a \approx 1$  V we observe a single emission line [Fig. 2(b)] with full-width-at-half-maximum (FWHM) linewidth of 1.4(2) GHz, near the spectrometer resolution of  $\sim 0.9$  GHz. We interpret this peak as containing unresolved contributions from the  $|E_{x,y}\rangle \rightarrow |0\rangle$  cycling transitions [39, 40]. Taking into consideration the absence of other peaks, in particular the  $|A_2\rangle \rightarrow |\pm 1\rangle$  cycling transition [23], and the observed noise floor, we place a bound on the ground-state spin polarization  $\mathcal{P}_{GS} \equiv P_0/(P_0 + P_{\pm 1}) \gtrsim 90\%$ , where  $P_i$  is the occupation probability of state  $|i\rangle$ .

Upon application of transverse fields, the spin character of the levels in the upper  $|\mathcal{E}_x\rangle$  orbital branch,  $\{|A_2\rangle, |A_1\rangle, |E_x\rangle\}$ , remain relatively unperturbed. In contrast, the spin character of levels in  $|\mathcal{E}_y\rangle$ ,  $\{|E_y\rangle, |E_1\rangle, |E_2\rangle\}$ , mix at avoided crossings due to spin-spin interaction [30, 31, 39, 41], making these levels useful for spin-altering  $\Lambda$  schemes.

For  $5 \text{ V} \lesssim V_a \lesssim 35 \text{ V}$ , three emission lines are visible [inset of Fig. 2(a)]. Based on the positive, linear tuning, the upper peak is identified as  $|E_x\rangle \rightarrow |0\rangle$ . Lorentzian fits to these spectra reveal that the two lowest lines are on average separated by 2.7(2) GHz, which is comparable to  $D_{GS}$ . Based on this peak separation and the negative, linear tuning, we conclude that these peaks arise from  $|\mathcal{E}_y\rangle \rightarrow |0\rangle$  and  $|\mathcal{E}_y\rangle \rightarrow |\pm 1\rangle$  emission. In this region, the three levels within  $|\mathcal{E}_y\rangle$  are nearly degenerate and unresolved here. The presence of these lines was previously predicted from work on spin-altering  $\Lambda$  transitions involving the lower orbital branch [39, 41, 42]. Figure 2(c) plots the emission frequencies along with a fit to the expected transition frequencies computed using a model based on Eq. (1), showing excellent agreement. The fitted parameters are  $d_{\parallel}F_{\parallel}/V_a = 0.42(2) \text{ GHz/V}$  and  $d_{\perp}F_{\perp}/V_a = 1.03(3) \text{ GHz/V}$ .

Even when there is significant emission to  $|\pm 1\rangle$ , we still do not observe  $|A_2\rangle \rightarrow |\pm 1\rangle$  emission. Throughout, we find  $\mathcal{P}_{GS} \gtrsim 85\%$ , where the difference from the bound on polarization at  $V_a \approx 1$  V is only due to lower signal-to-noise ratio. A likely explanation is that any population in  $|\pm 1\rangle$  is quickly transferred to the metastable singlet levels [43], preventing the detection of  $m_s = \pm 1$  emission lines. This is consistent with Fig. 2(d), where the total ZPL emission rate integrated over all lines is plotted as a function of one half the orbital splitting,  $\delta_{\perp}$ . Between  $3 \lesssim \delta_{\perp} \lesssim 10 \text{ GHz}$

( $3 \lesssim V_a \lesssim 10 \text{ V}$ ), the emission rate falls precipitously before leveling off at about half the initial rate. This behavior motivates operating at near-zero transverse field for applications where maximizing emission rate is critical.

The relative intensity of the emission lines gives further insight into the ES properties. Figure 2(e) plots the intensity of the  $|\mathcal{E}_y\rangle \rightarrow |\pm 1\rangle$  emission line, normalized by the total emission from  $|\mathcal{E}_y\rangle$ , as a function of  $\delta_{\perp}$ . Evidently, the applied field is a powerful knob in tuning the relative transition strengths in this  $\Lambda$  system. This feature can be used to optimize quantum information protocols [6, 44]. Two peaks for the emission of  $|\mathcal{E}_y\rangle \rightarrow |\pm 1\rangle$  are present at  $\delta_{\perp} \approx 7$  and 15 GHz. These features correspond to level anticrossings [see Fig. 1(c)], where maximal mixing of levels in the lower orbital branch occurs. The degree of mixing depends sensitively on both the magnitude of the transverse electric field and its angle,  $\theta_r$ , with respect to the  $C_{3v}$  reflection planes [39]. We model the relative emission intensity by assuming the NV center is excited from  $|0\rangle$  to one of the three levels in the lower branch,  $|\mathcal{E}_{y,i}\rangle$ , weighted by the probability of  $m_s = 0$  projection,  $P_{0,i}(\theta_r, \delta_{\perp}) = |\langle \tilde{E}_x | \mathcal{E}_{y,i} \rangle|^2 + |\langle \tilde{E}_y | \mathcal{E}_{y,i} \rangle|^2$ . Here  $\tilde{E}_{x,y}$  are eigenstates of  $\mathcal{H}_{SO}$  alone, which contain purely  $m_s = 0$  projection. The probability that emission is back to  $|\pm 1\rangle$  is then  $\sum_i P_{0,i}(\theta_r, \delta_{\perp})(1 - P_{0,i}(\theta_r, \delta_{\perp}))$ . Using the model based on Eq. (1), we fit this formula to the data and find good agreement for  $\theta_r = 15(5)^\circ$ .

Finally, we also observe a strong dependence of the relative emission between the upper and lower branches on  $\delta_{\perp}$  [Fig. 2(a)]. Given the low temperature  $T = 7 \text{ K}$ , this may be due to a single-phonon orbital relaxation process. A detailed study will be the focus of future work. All of the effects described above were reproduced in subsequent voltage scans [Supplementary Information].

To realize even higher spectral resolution, we performed photoluminescence excitation (PLE) spectroscopy. Attenuated light ( $\sim 60 \text{ nW}$ ) from a tunable, extended-cavity diode laser ( $\sim 637 \text{ nm}$ ) was used for ZPL excitation, and the collected light was spectrally filtered to direct the PSB emission (650-800 nm) to a single-photon-counting detector (SPCD). A microwave field resonant with the ground-state spin transition,  $D_{GS} = 2.877 \text{ GHz}$ , was continuously applied to counteract optical pumping [39, 45], and light from a repump laser (532 nm) was pulsed by an acousto-optic modulator and strategically employed to reverse photoionization [42, 46, 47].

Figure 3(a) plots PLE spectra for NV1 as a function of  $V_a$ , applied simultaneously to  $V_{\text{ref}}$  and  $V_1$ , with  $V_2 = 0$ . Multiple excitation lines are resolved, including a few transitions not observed in emission spectroscopy, due to the presence of resonant microwave excitation. We fit the five strongest lines with Lorentzian profiles. The extracted peak positions are plotted in Fig. 3(b)

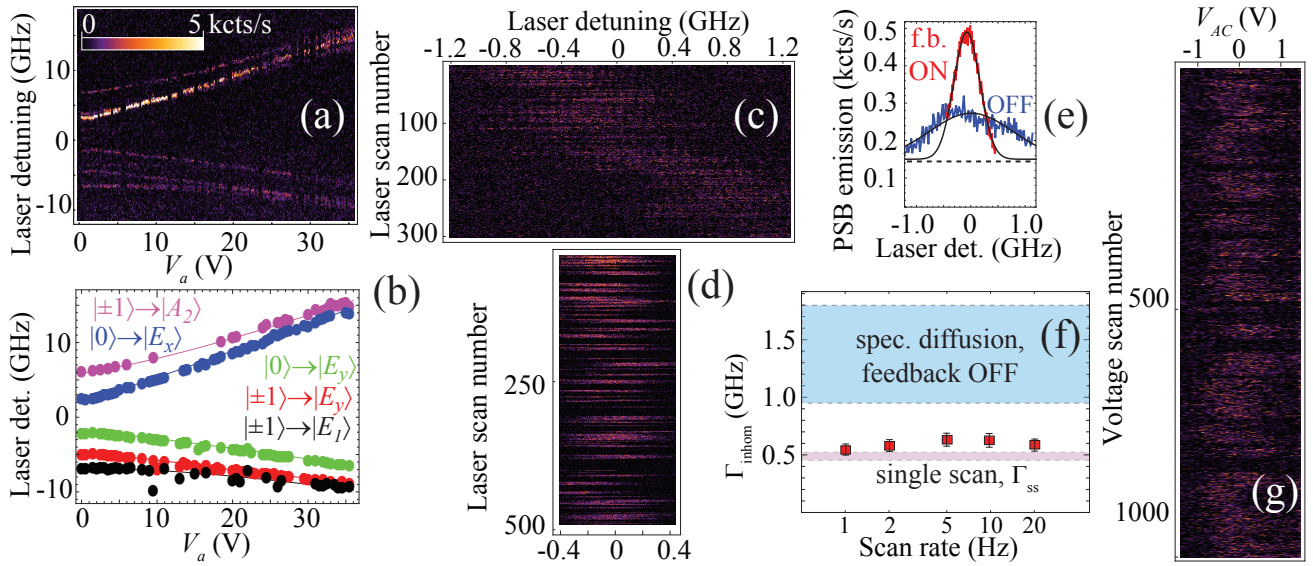


FIG. 3. (a) PLE spectra versus applied voltage for NV1. A 532 nm repump pulse (2.5  $\mu$ W, 1 s duration) was applied every 60 s. (b) Fitted transition frequencies from (a) and global fit to the model based on Eq. (1), with transitions labeled. (c) PLE spectra for NV2 ( $|0\rangle \rightarrow |E_x\rangle$ ) with  $V_a = -4$  V. The scan rate was 1 Hz, and a repump pulse (10  $\mu$ W, 0.1 s) was applied during every back-scan. (d) PLE spectra for NV2 with voltage feedback applied. The enhanced spectral stability allowed us to reduce the laser-frequency scan range by a factor of four. (e) Sum over the scans in (c) and (d) with, respectively, feedback off (blue) and on (red) along with Gaussian fits (solid black lines) using the mean background of 150 cts/s (black dashed line). (f) Comparison of  $\Gamma_{\text{inhom}}$  as a function of scan repetition rate. The spectral-diffusion-broadened linewidth (blue shaded region) is the range observed over data sets taken without feedback with 1, 2, 5, 10 and 20 Hz scan rates. (g) 100 s segment of PLE spectra obtained by rapidly scanning a voltage,  $V_{AC}$ , with feedback applied to  $V_{DC}$ . The laser frequency was constant to within 20 MHz throughout the measurement.

along with a global fit to the model based on Eq. (1), yielding Stark coefficients  $d_{\parallel}F_{\parallel}/V_a = 0.11(1)$  GHz/V and  $d_{\perp}F_{\perp}/V_a = 0.26(2)$  GHz/V. These coefficients are about four times smaller than those realized under strong 532 nm excitation, consistent with previous observations of enhanced electrical tuning due to photoionization effects [1, 2].

In addition to static control over optical transition frequencies and strengths, electric tuning can be used to provide dynamic compensation for fluctuating local fields. These fluctuations lead to spectral diffusion of the ZPL frequencies [22, 27], a significant challenge for optical resonance studies [2, 23, 25, 26]. For the NV center, a likely cause for spectral diffusion is photoionization of nearby defects; this effect may be magnified due to other charging effects in the presence of applied voltages [1].

To investigate these faster dynamics, we use PLE spectroscopy on the  $|0\rangle \rightarrow |E_x\rangle$  transition of NV2. Figure 3(c) shows typical PLE spectra when scanning the excitation laser frequency through resonance and applying a repump after each scan. The average linewidth for single scans, computed using the technique in Ref. [38], was  $\Gamma_{\text{ss}} = 0.48(8)$  GHz for NV2. For NV1, we observed  $\Gamma_{\text{ss}} = 0.14(3)$  GHz. In both cases,  $\Gamma_{\text{ss}}$  is more than an order of magnitude broader than the natural linewidth,  $\Gamma_{\text{nat}} \approx 13$  MHz, and is independent of scan repetition rate in the range studied here (1-20 Hz). This property

requires further investigation, as  $\Gamma_{\text{ss}} \approx \Gamma_{\text{nat}}$  has been observed in other samples for NV centers located several  $\mu$ m below the surface [2, 14, 38]. Nonetheless, the ZPL center frequency in Fig. 3(c) drifts over a range significantly larger than  $\Gamma_{\text{ss}}$  during the 300 s data set.

Our solution to the spectral-drift problem is to actively adjust  $V_a$  to compensate for the changing local field. We start with  $V_a = -4$  V, and, during the back-scan of subsequent scans (final 10% of each cycle), we employ software-controlled feedback with the following algorithm. We first determine the position and intensity of the peak fluorescence. If the intensity falls below a threshold, we apply a repump pulse and do not change  $V_a$ . Otherwise, we change  $V_a$  based on optimized proportionality and integration inputs [Supplementary Information].

Figure 3(d) shows PLE spectra under similar conditions as Fig. 3(c) but now with feedback applied. While  $\Gamma_{\text{ss}}$  remains unchanged, the center-frequency drift is substantially reduced. A figure of merit for the spectral drift of the transition is obtained by summing over many PLE scans and determining the resulting inhomogeneous linewidth,  $\Gamma_{\text{inhom}}$ . Figure 3(e) compares the sum of spectra with feedback off [Fig. 3(c)] and on [3(d)] along with Gaussian fits. Without feedback, we find  $\Gamma_{\text{inhom}} = 1.8(2)$  GHz  $\approx 3.8\Gamma_{\text{ss}}$ , and with feedback this decreases to  $0.54(4)$  GHz  $\approx 1.1\Gamma_{\text{ss}}$ .

This feedback technique can be applied at signifi-



cantly higher bandwidth without compromising stability. Figure 3(f) plots  $\Gamma_{\text{inhom}}$  as a function of scan repetition rate up to 20 Hz. Throughout this range, we find  $\Gamma_{\text{inhom}} \lesssim 1.3\Gamma_{\text{ss}}$ . Similar results were obtained for NV1 as well as for stabilizing the  $|\pm 1\rangle \rightarrow A_2$  transition.

It is often advantageous to perform experiments with the excitation laser frequency fixed to an external reference. In this case, voltage feedback can still be employed by modulating the ZPL transition frequency using an AC voltage,  $V_{AC}$ , and providing stabilizing feedback to the DC component,  $V_{DC}$ . With this technique, feedback can be applied continuously without substantially degrading photon indistinguishability, provided that the modulation depth and laser linewidth are sufficiently small.

Figure 3(e) shows results of locking the NV2  $|0\rangle \rightarrow |E_x\rangle$  transition frequency using only applied voltages. We apply  $V_{AC}$ , a ramp waveform of amplitude  $3 V_{\text{pp}}$  and period 0.1 s, to  $V_2$  and  $V_{\text{ref}}$ . Meanwhile,  $V_{DC}$  is fed back to  $V_1$ , initially starting at  $-8$  V, but varying by  $\sim \pm 4$  V throughout the 600 s measurement. After subtracting the 150 cts/s background, we collect on average 144 cts/s. This compares favorably to the 34 cts/s collected without feedback (with repump applied every scan). The overall count rate can be further increased with improved collection efficiency [48, 49] and resonant ZPL enhancement [28].

In summary, we have used the Stark effect to electrically tune and stabilize the structure of the NV center's excited state and probe the coupling to its local environment. The techniques presented here should dramatically improve the entanglement success probability in quantum communications protocols. In order to completely eliminate inhomogeneous broadening, further work is necessary to understand and control more rapid broadening mechanisms [50].

We acknowledge support by the Defense Advanced Research Projects Agency (award no. HR0011-09-1-0006), the Regents of the University of California, and the Australian Research Council (ARC) (Project Nos. LP100100524, DP1096288, and DP0880466). We thank T. Karle, B. Gibson, K. Ganesan, T. Ishikawa, B. Buckley, and A. Falk for valuable discussions.

---

\* victor.acosta@hp.com

- [1] J. L. O'Brien, *Science* (New York, N.Y.) **318**, 1567 (2007).
- [2] A. M. Stephens, Z. W. E. Evans, S. J. Devitt, A. D. Greentree, A. G. Fowler, W. J. Munro, J. L. O'Brien, K. Nemoto, and L. C. L. Hollenberg, *Physical Review A* **78**, 032318 (2008).
- [3] S. Benjamin, B. Lovett, and J. Smith, *Laser & Photonics Review* **3**, 556 (2009).
- [4] T. D. Ladd, F. Jelezko, R. Laflamme, Y. Nakamura, C. Monroe, and J. L. O'Brien, *Nature* **464**, 45 (2010).
- [5] C. Santori, P. E. Barclay, K.-M. C. Fu, R. G. Beausoleil, S. Spillane, and M. Fisch, *Nanotechnology* **21**, 274008 (2010).
- [6] C. Cabrillo, J. I. Cirac, P. García-Fernández, and P. Zoller, *Physical Review A* **59**, 1025 (1999).
- [7] L. I. Childress, J. M. Taylor, A. Sørensen, and M. D. Lukin, *Physical Review A* **72**, 052330 (2005).
- [8] D. L. Moehring, P. Maunz, S. Olmschenk, K. C. Younge, D. N. Matsukevich, L.-M. Duan, and C. Monroe, *Nature* **449**, 68 (2007).
- [9] M. Orrit, J. Bernard, A. Zumbusch, and R. Personov, *Chemical Physics Letters* **196**, 595 (1992).
- [10] U. P. Wild, F. Güttler, M. Pirotta, and A. Renn, *Chemical Physics Letters* **193**, 451 (1992).
- [11] R. Lettow, Y. L. A. Rezus, A. Renn, G. Zumofen, E. Ikonen, S. Götzinger, and V. Sandoghdar, *Physical Review Letters* **104**, 123605 (2010).
- [12] S. A. Empedocles and M. G. Bawendi, *Science* **278**, 2114 (1997).
- [13] R. B. Patel, A. J. Bennett, I. Farrer, C. A. Nicoll, D. A. Ritchie, and A. J. Shields, *Nature Photonics* **4**, 632 (2010).
- [14] P. Tamarat, T. Gaebel, J. R. Rabeau, M. Khan, A. D. Greentree, H. Wilson, L. C. L. Hollenberg, S. Praver, P. Hemmer, F. Jelezko, and J. Wrachtrup, *Physical Review Letters* **97**, 083002 (2006).
- [15] L. Bassett, F. Heremans, and C. Yale, (2011), arXiv:1104.3878v1.
- [16] H. Bernien, L. Childress, and L. Robledo, (2011), arXiv:1110.3329v1.
- [17] W. P. Ambrose and W. E. Moerner, *Nature* **349**, 225 (1991).
- [18] F. Jelezko, B. Lounis, and M. Orrit, *The Journal of Chemical Physics* **107**, 1692 (1997).
- [19] C. Santori, D. Fattal, J. Vučković, G. S. Solomon, and Y. Yamamoto, *Nature* **419**, 594 (2002).
- [20] A. D. Greentree, P. Olivero, M. Draganski, E. Trajkov, J. R. Rabeau, P. Reichart, B. C. Gibson, S. Rubanov, S. T. Huntington, D. N. Jamieson, and S. Praver, *Journal of Physics: Condensed Matter* **18**, S825 (2006).
- [21] S. Ates, S. M. Ulrich, S. Reitzenstein, A. Löffler, A. Forchel, and P. Michler, *Physical Review Letters* **103**, 167402 (2009).
- [22] L. Robledo, H. Bernien, I. van Weperen, and R. Hanson, *Physical Review Letters* **105**, 177403 (2010).
- [23] E. Togan, Y. Chu, A. S. Trifonov, L. Jiang, J. Maze, L. Childress, M. V. G. Dutt, A. S. Sørensen, P. R. Hemmer, A. S. Zibrov, and M. D. Lukin, *Nature* **466**, 730 (2010).
- [24] G. Balasubramanian, P. Neumann, D. Twitchen, M. Markham, R. Kolesov, N. Mizuochi, J. Isoya, J. Achard, J. Beck, J. Tissler, V. Jacques, P. R. Hemmer, F. Jelezko, and J. Wrachtrup, *Nat Mater* **8**, 383 (2009).
- [25] B. B. Buckley, G. D. Fuchs, L. C. Bassett, and D. D. Awschalom, *Science* (New York, N.Y.) **330**, 1212 (2010).
- [26] L. Robledo, L. Childress, H. Bernien, B. Hensen, P. F. A. Alkemade, and R. Hanson, *Nature* **477**, 574 (2011).
- [27] K. M. C. Fu, C. Santori, P. E. Barclay, and R. G. Beausoleil, *Applied Physics Letters* **96**, 121903 (2010).
- [28] A. Faraon, P. E. Barclay, C. Santori, K.-M. C. Fu, and R. G. Beausoleil, *Nature Photonics* **5**, 301 (2011).
- [29] V. M. Acosta, E. Bauch, M. P. Ledbetter, A. Waxman, L. S. Bouchard, and D. Budker, *Physical Review Letters* **104**, 70801 (2010).
- [30] M. W. Doherty, N. B. Manson, P. Delaney, and L. C. L.

- Hollenberg, *New Journal of Physics* **13**, 25019 (2011).
- [31] J. Maze, A. Gali, E. Togan, Y. Chu, A. S. Trifonov, E. Kaxiras, and M. D. Lukin, *New Journal of Physics* **13**, 25025 (2011).
  - [32] A. E. Hughes and W. A. Runciman, *Proceedings of the Physical Society* **90**, 827 (1967).
  - [33] G. Davies and M. F. Hamer, *Proceedings of the Royal Society A: Mathematical, Physical and Engineering Sciences* **348**, 285 (1976).
  - [34] E. van Oort and M. Glasbeek, *Chemical Physics Letters* **168**, 529 (1990).
  - [35] F. Dolde, H. Fedder, M. Doherty, T. Nöbauer, F. Rempp, G. Balasubramanian, T. Wolf, F. Reinhard, L. Hollenberg, F. Jelezko, and Others, *Nature Physics* **7**, 459 (2011).
  - [36] A. Stacey, D. A. Simpson, T. J. Karle, B. C. Gibson, V. Acosta, Z. Huang, K.-M. C. Fu, C. Santori, R. G. Beausoleil, L. P. McGuinness, K. Ganesan, S. Tomljenovic-Hanic, A. D. Greentree and S. Prawer, in preparation (2012).
  - [37] A. Stacey, T. J. Karle, L. P. McGuinness, B. C. Gibson, K. Ganesan, S. Tomljenovic-Hanic, A. D. Greentree, S. Prawer, R. G. Beausoleil, and A. Hoffman, (2011), arXiv:1108.6078.
  - [38] K.-M. C. Fu, C. Santori, P. E. Barclay, L. J. Rogers, N. B. Manson, and R. G. Beausoleil, *Physical Review Letters* **103**, 256404 (2009).
  - [39] P. Tamarat, N. B. Manson, J. P. Harrison, R. L. McMurtrie, A. Nizovtsev, C. Santori, R. G. Beausoleil, P. Neumann, T. Gaebel, F. Jelezko, P. Hemmer, and J. Wrachtrup, *New Journal of Physics* **10**, 045004 (2008).
  - [40] A. Batalov, V. Jacques, F. Kaiser, P. Siyushev, P. Neumann, L. J. Rogers, R. L. McMurtrie, N. B. Manson, F. Jelezko, and J. Wrachtrup, *Physical Review Letters* **102**, 195506 (2009).
  - [41] C. Santori, D. Fattal, S. M. Spillane, M. Fiorentino, R. G. Beausoleil, A. D. Greentree, P. Olivero, M. Dragan-ski, J. R. Rabeau, P. Reichart, B. C. Gibson, S. Rubanov, D. N. Jamieson, and S. Prawer, *Optics Express* **14**, 7986 (2006).
  - [42] C. Santori, P. Tamarat, P. Neumann, J. Wrachtrup, D. Fattal, R. G. Beausoleil, J. Rabeau, P. Olivero, A. D. Greentree, S. Prawer, F. Jelezko, and P. Hemmer, *Physical Review Letters* **97**, 247401 (2006).
  - [43] V. M. Acosta, A. Jarmola, E. Bauch, and D. Budker, *Physical Review B* **82**, 201202 (2010).
  - [44] L. M. Duan, M. D. Lukin, J. I. Cirac, and P. Zoller, *Nature* **414**, 413 (2001).
  - [45] F. Jelezko, I. Popa, A. Gruber, C. Tietz, J. Wrachtrup, A. Nizovtsev, and S. Kilin, *Applied Physics Letters* **81**, 2160 (2002).
  - [46] A. Drabenstedt, L. Fleury, C. Tietz, F. Jelezko, S. Kilin, A. Nizovtzev, and J. Wrachtrup, *Physical Review B* **60**, 11503 (1999).
  - [47] G. Waldherr, J. Beck, M. Steiner, P. Neumann, A. Gali, T. Frauenheim, F. Jelezko, and J. Wrachtrup, *Physical Review Letters* **106**, 157601 (2011).
  - [48] J. P. Hadden, J. P. Harrison, A. C. Stanley-Clarke, L. Marseglia, Y. L. D. Ho, B. R. Patton, J. L. O'Brien, and J. G. Rarity, *Applied Physics Letters* **97**, 241901 (2010).
  - [49] B. J. M. Hausmann, B. Shields, Q. Quan, P. Maletinsky, M. McCutcheon, J. T. Choy, T. M. Babinec, A. Kubanek, A. Yacoby, M. D. Lukin, and M. Loncar, (2011), arXiv:1111.5330.
  - [50] G. Sallen, A. Tribu, T. Aichele, R. André, L. Besombes, C. Bougerol, M. Richard, S. Tatarenko, K. Kheng, and J.-P. Poizat, *Nature Photonics* **4**, 696 (2010).

# Supplementary Information: Dynamic stabilization of the optical resonances of single nitrogen-vacancy centers in diamond

## ELECTROSTATIC MODELING

We modeled the electric field produced by the electrode structure in Fig. 1(c) of the main text using the COMSOL MULTIPHYSICS® electrostatics package. The bottom layer of each electrode is composed of 10 nm of Ti, so for simplicity we model the electrodes as being 100-nm thick, composed entirely of Ti. We use a relative permittivity for the diamond substrate  $\epsilon_r = 5.1$ . The positions of NV1 and NV2 were determined by fluorescence micrographs, as in Fig. 1(d) of the main text.

Based on our simulations, application of 10 V to one electrode (with the other two electrodes grounded) corresponds to an electric field amplitude at the location of NV1 of 0.9, 0.6, and 1.1 MV/m, for  $V_1$ ,  $V_2$ , and  $V_{\text{ref}}$ , respectively. In Fig. S1 we plot the in-plane electric field components on the diamond surface for  $\{V_1, V_2, V_{\text{ref}}\} = \{10, 0, 10\}$  V.

As a note of caution: this model assumes a perfect dielectric response. In reality the local field is subject to significant deviations due to charge variations introduced by the electrodes or from photo-ionization [S1]. These deviations do not substantially affect the performance of dynamic ZPL stabilization, since the proportional gain can be adjusted to compensate (see below), but they do play an important role in static tuning. One example is the photo-induced effect that is responsible for the  $\sim 4$  times greater Stark tuning coefficients for strong (2 mW) cw green excitation, compared with weak ( $\sim 60$  nW) red excitation, and is discussed in detail in Ref. [S1].

We also observe hysteretic charging effects which alter the static tuning even with very weak ( $\lesssim 60$  nW) red excitation and without applying any green repump. This hysteresis results in a variation of observed tuning coefficients which depends on scan direction, rate, and history. The variation exists even between successive voltage scans as short as 10 s. Overall, the observed tuning coefficients vary by up to a factor of 5, making a measurement of the intrinsic dipole moment of the NV center a difficult task. Using the Stark tuning coefficients for NV1, determined from the  $\sim 2$  hr forward voltage scan in Fig. 3(a) of the main text, the dipole moment is  $\{d_{\parallel}, d_{\perp}\} \approx \{4, 5\}$  GHz/MV/m, which is probably correct to within a factor of 2-3. For this calculation the magnitude of the applied electric field and its angle with respect to the NV axis were estimated based on the electrostatic modeling in Fig. S1 and the dependence of NV1 fluorescence intensity on excitation light polarization.

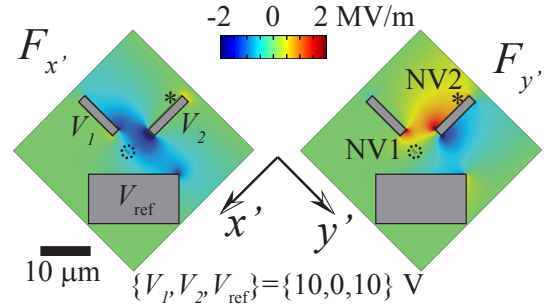


FIG. S1. In-plane electric-field components on the diamond surface,  $F_{x',y'}$ , for  $V_a = 10$  V applied simultaneously to  $V_1$  and  $V_{\text{ref}}$ , with  $V_2 = 0$ . The locations of NV1 (dashed circle) and NV2 (asterisk) are shown, as in Fig. 1 of the main text. The out-of-plane component  $F_{z'} \approx 0$ .

## REPRODUCIBILITY OF EMISSION SPECTROSCOPY

The reproducibility of Stark emission spectroscopy results was tested by varying the voltage on various combinations of electrodes. Figure S2(a) shows emission spectra while varying the voltage applied to  $V_1$ , with  $V_2 = V_{\text{ref}} = 0$ . Despite the continuous voltage tuning, small kinks in the emission lines are observed, particularly following dark frames. During the dark frames of this particular data set, we performed a peak-finding procedure that locates the optical focal position which produces maximum NV emission. The resulting shifts in optical focus may produce small changes in the local field due to photo-induced charge redistribution [S1, S2]. In Fig. 2 of the main text we used a different procedure to maintain optical focus based on continuous feedback using a weak white-light reflection image. This may explain the absence of sharp kinks in the Stark emission spectra in Fig. 2(a).

The inset of Fig. S2(a) shows the low-field spectra, with three emission lines clearly visible. As in Fig. 2 of the main text, we do not observe  $|A_2\rangle \rightarrow |\pm 1\rangle$  emission, indicating ground-state spin polarization,  $\mathcal{P}_{GS} \gtrsim 85\%$ . Following the procedure outlined in the main text, we fit these spectra [Fig. S2(b)] and found Stark coefficients of  $d_{\parallel} F_{\parallel}/V_a = 0.26(2)$  GHz/V and  $d_{\perp} F_{\perp}/V_a = 0.81(4)$  GHz/V. In Fig. S2(c), the total emission intensity as a function of  $\delta_{\perp}$  is plotted. These data are qualitatively similar to that found in Fig. 2(d) of the main text. In Fig. S2, the emission intensity of the  $|\mathcal{E}_y\rangle \rightarrow |\pm 1\rangle$  line, relative to the total emission from  $|\mathcal{E}_y\rangle$ , is plotted versus  $\delta_{\perp}$ . Based on the fit, we find  $\theta_r = 12(5)^\circ$ .

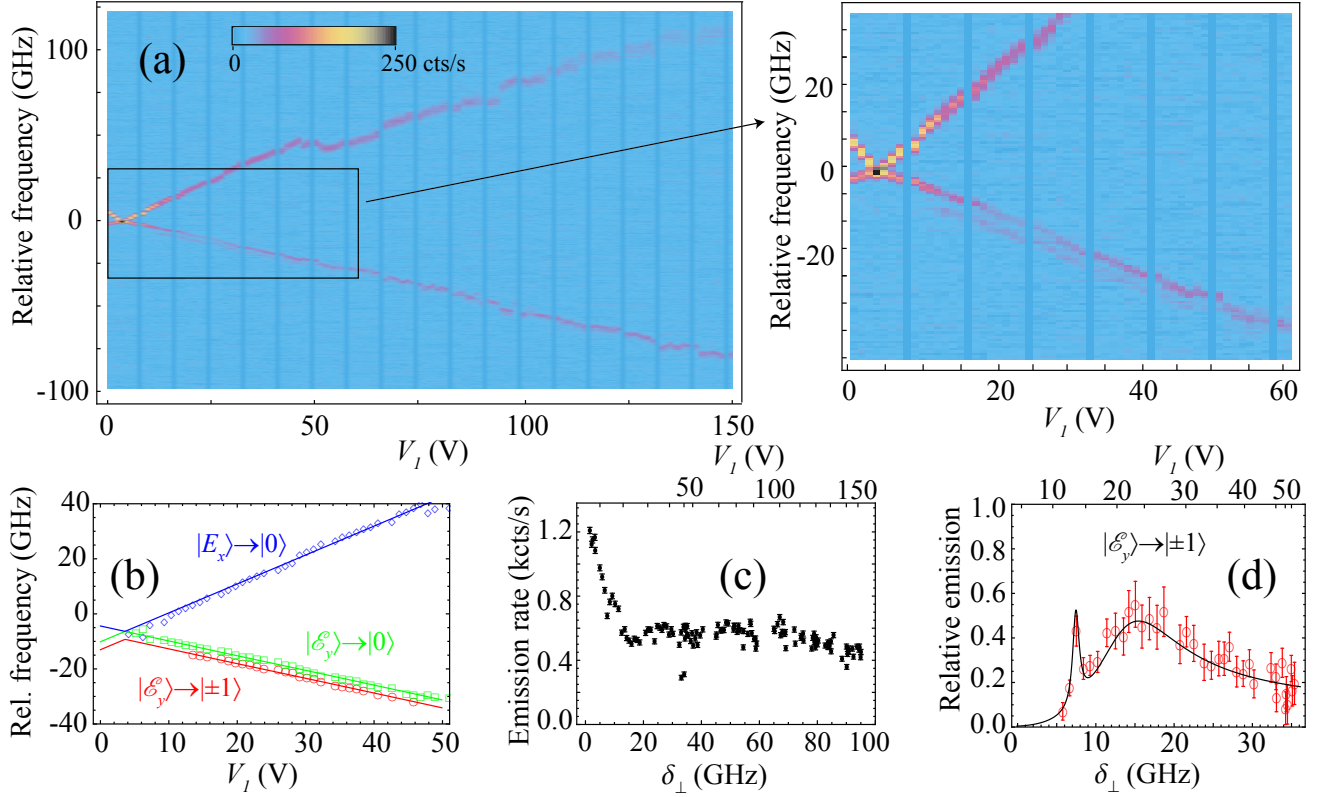


FIG. S2. (a) Stark emission spectra as a function of applied voltage on  $V_1$ , with  $V_2 = V_{\text{ref}} = 0$ . Low-field data are inset. (b) Low-field peak positions determined from Lorentzian fits (symbols) and global fit. Lorentzian fit uncertainty is smaller than the plotted symbols. (c) Total ZPL emission versus  $\delta_{\perp}$ . (d) Relative intensity of the  $|\mathcal{E}_y\rangle \rightarrow |\pm 1\rangle$  emission line along with fit. The methods for fitting and processing spectra are described in the main text.

### FEEDBACK OPTIMIZATION

The basic feedback protocol is described in the text and here we outline experimental details. All PLE scans used a ramp waveform with 90% duty cycle. In other words, we scan either the laser frequency or  $V_{AC}$  in one direction for 90% of the total scan cycle and the final 10% is devoted to scanning back in the other direction (the “back-scan”). We divide our collected PSB counts into bins of variable size, typically forming 10-50 bins in total. During the backscan of each cycle (denoted with index  $i$ ), we search for the bin location,  $b_i$ , with the maximum counts,  $C_i$ . We set a threshold,  $T$ , typically corresponding to a count rate of 1 kcts/s. If  $C_i < T$ , we apply a green repump pulse for the remainder of the backscan and do not change  $V_{DC}$ .

If  $C_i \geq T$ , we do not apply a repump pulse. Instead, we change  $V_{DC}$  by an amount  $\delta V_i$  using the following formula:

$$\delta V_i = G \times \left( B - \frac{1}{N} \sum_{j=0}^{N-1} b_{i-j} \right). \quad (\text{S1})$$

Here  $G$  is a gain factor,  $N$  is an integration factor corresponding to the number of cycles used to determine  $\delta V_i$ , and  $B$  is the desired peak position. In our experiments, we typically set  $B$  to be the bin at the center of each scan. For all of the laser-frequency scans in the main text [Fig. 3(c)-(f)], we used  $N = 1$  (no integration). For the 0.1-s voltage scans we found that feedback was most efficient using  $N = 2-4$ . The 100-second portion shown in Fig. 3(g) used  $N = 2$ . We separately optimize  $G$  based on the NV center’s Stark tuning coefficients as well as the method and rate of scanning.

---

\* victor.acosta@hp.com

[S1] L. Bassett, F. Heremans, and C. Yale, (2011), arXiv:1104.3878v1.

[S2] H. Bernien, L. Childress, and L. Robledo, (2011), arXiv:1110.3329v1.